13th International Symposium on Particle Image Velocimetry – ISPIV 2019
Munich, Germany, July 22-24, 2019

Instantaneous self-calibration of a 3D imaging system in industrial facility with strong vibrations

Matteo Novara, Daniel Schanz, Reinhard Geisler, Sebastian Gesemann, Florian Philipp, Janos Agocs, Andreas Schröder

German Aerospace Center (DLR), Institute of Aerodynamics and Flow Technology, Göttingen, Germany

* matteo.novara@dlr.de

Abstract

The flow on the suction side of a half-wing model is investigated by means of 3D Lagrangian particle tracking (LPT) with Multi-Pulse Shake-The-Box and stereoscopic particle image velocimetry. The experiment is carried out in the Low Speed Wind-Tunnel facility (LSWT) at the Airbus UK site (Filton, England). Illumination is provided by a multi-pulse system consisting of two dual-pulse lasers. A 3D imaging system is composed of five double-frame cameras; a two-camera subset can be employed in stereoscopic fashion. Due to the constrains posed by the limited optical access to the measurement region, three cameras are installed inside the wind-tunnel test section. As a consequence, significant vibrations occur during the operation of the wind-tunnel, leading to large unsteady decalibration of the imaging system (up to 120 px). A tailored single-snapshot self-calibration approach is proposed here which makes use of standard volume self-calibration and particle triangulation from the 3D imaging system to detect and correct the camera decalibration for each instantaneous recording. Results shows that the disparity error can be reduced to less than 0.1 px, a suitable value for both accurate 3D particle triangulation using the full imaging system and for stereoscopic evaluation of the out-of-plane velocity component with PIV making use of a two-camera subset.

1 Introduction

Volume self-calibration (VSC, Wieneke (2008)) is a technique developed to correct mapping function errors of a multi-camera imaging system making use of actual particle image recordings. Decalibration errors typically occur due to inaccurate calibration targets, inaccurate target positioning or movement, mechanical instabilities or optical distortions not accounted for by the mapping function. The use of VSC has become common practice for experimental investigations carried out by means of 3D imaging systems, such as Tomographic-PIV (Tomo-PIV, Elsinga et al. (2006)) and Shake-The-Box (STB, Schanz et al. (2016)), where a sub-pixel mapping accuracy is required for the successful reconstruction/triangulation of the particle location within the investigated 3D volume.

The VSC technique is based on the detection of particle peaks on the 2D recordings, followed by the triangulation of the particle positions in the 3D space; the maximum allowed triangulation error needs to be larger than the expected decalibration error in order to successfully triangulate the 3D particle locations. The reconstructed particles are then back-projected onto the camera image plane; the distance between the back-projected location and the recorded particle image peak provides an indication of the decalibration error for each particle (i.e. disparity). The 3D volume is typically partitioned into several sub-volumes and, for each camera and sub-volume, individual disparities are collected into disparity maps. A clustering method ensures that the actual particles build a coherent peak in the disparity maps, while disparities from spurious particles (*ghost particles*, Elsinga et al. (2011)) contribute to the noise. The location of the disparity peaks provides a disparity vector map that can be used to correct the mapping function. An iterative approach is commonly adopted, where the maximum allowed triangulation error is progressively reduced and the number of sub-volumes increased in order to capture spatially varying calibration errors. After successfully applying VSC, the residual disparity is typically reduced to sub-pixel values ($0.1-0.2\,px$, Wieneke (2008)).

In order to increase the signal-to-noise ratio of the disparity maps, an ensemble approach is typically employed where the disparity maps from a sequence of recordings are summed. As a consequence, it is common practice to record a number of particle images (typically 50 to 100 recordings) dedicated to

VSC before (and after) the actual measurement images are acquired. Dedicated VSC images are typically recorded at low particle image density ($\leq 0.02\,ppp$, particles per pixel) in order to reduce the number of triangulated ghost particles and further improve the signal-to-noise ratio.

This ensemble approach cannot be adopted when unsteady decalibration errors occur. This is a common situation in many industrial and aerodynamics applications where relatively fast flows are investigated in large facilities; as a consequence, structural vibrations potentially result in unsteady camera displacements and the VSC correction needs to be applied for each instantaneous recording (Michaelis and Wolf (2011), Novara et al. (2016b)). Furthermore, the instantaneous correction has to be detected based on the analysis of actual particle images, typically exhibiting higher values in terms of particle image density (up and exceeding $0.05\,ppp$ for Tomo-PIV and STB investigations).

As a consequence, due to the limited statistics offered by single images, the disparity maps are characterized by low signal-to-noise values. This condition is exacerbated when strong camera vibrations are encountered and a large triangulation error (e.g. $> 5\,px$) must be allowed for the 3D particle triangulation to work. Here, alongside with the actual particles, a large number of ghost particles is generated, which contribute to increasing the noise level in the disparity maps, eventually hiding the actual disparity peak.

A single-image approach for the volume self-calibration correction has been proposed by Michaelis and Wolf (2011). A first VSC iteration is performed over the complete volume in order to detect a single disparity shift; subsequently, more detailed passes are applied with a reduced triangulation error and multiple sub-volumes until the residual disparity is reduced to sub-pixel values. In addition, only a portion of the brightest 2D peaks identified on the images is used for the triangulation process, which artificially reduces the particle image density and, as a consequence, the number of ghost particles.

Earl et al. (2014) investigated the issue of small unsteady decalibration errors that could potentially go unnoticed when performing VSC based on the ensemble averaging approach, while Cornic et al. (2016) worked on improving the correction scheme in case of camera drifts and mentioned the issue of the change of the origin of the coordinate system caused by the disparity correction.

Recently, Wieneke (2018) proposed two methods to further improve on the original implementation of the VSC in order to enhance its robustness in case of large decalibration errors and relatively high seeded images. The VSC with ghost particle suppression (VSC-GPS) is based on the fact that disparities from actual particles are located inside the true disparity peak, while spurious disparity values associated to ghost particles are randomly distributed across the map, unlikely to fall within the true disparity peak for every camera in the imaging system. This observation led to the implementation of a method to actively suppress the false information from the ghost particles, largely reducing the noise contribution in the disparity maps; this approach has been proven effective to compensate for decalibration errors up to approximately $10\,px$. The second approach (VSC-IC) is based on standard image correlation between dewarped images, similarly to what is done for stereo-PIV self-calibration (Wieneke (2005)). Since it does not rely on 2D peak detection and 3D triangulation, this method is particularly robust when dealing with highly seeded images and it has been successfully applied to identify single camera shifts up to $30\,px$. Typically, after correcting for these global shifts, a few iterations of standard VSC (or VSC-GPS) are employed in order to account for spatial gradients within the decalibration errors.

The present study deals with the calibration correction of a five-camera system employed for the investigation of a half-wing model in a large industrial facility. The significant structural vibration during wind-tunnel operation and the particular arrangement of the imaging system, together with the relatively high magnification and long distance of the cameras to the imaged volume, result in large unsteady decalibration errors, exceeding $100\,px$. An alternative single-snapshot correction method is presented here and applied to correct the decalibration error for each instantaneous recording. The method is tailored to the particular arrangement of the imaging system, where three of the five cameras are located within the test section, and it makes use of a single-image VSC approach, similar to what proposed by Michaelis and Wolf (2011), combined with the Iterative Particle Reconstruction technique (IPR, Wieneke (2013)) from a sub-set of cameras.

The experimental setup is described in section 2, while the several steps involved in the correction scheme are presented in section 3. Finally some results from the Multi-Pulse Shake-The-Box 3D Lagrangian particle tracking technique and stereo-PIV are shown in section 4, both concerning instantaneous results and flow statistics.

2 Experimental setup and imaging system calibration issues

The measurement is carried out in the Low Speed Wind-Tunnel facility (LSWT) at the Airbus UK site in Filton, England in the framework of a project contract for Airbus Operations LTD, aimed at providing

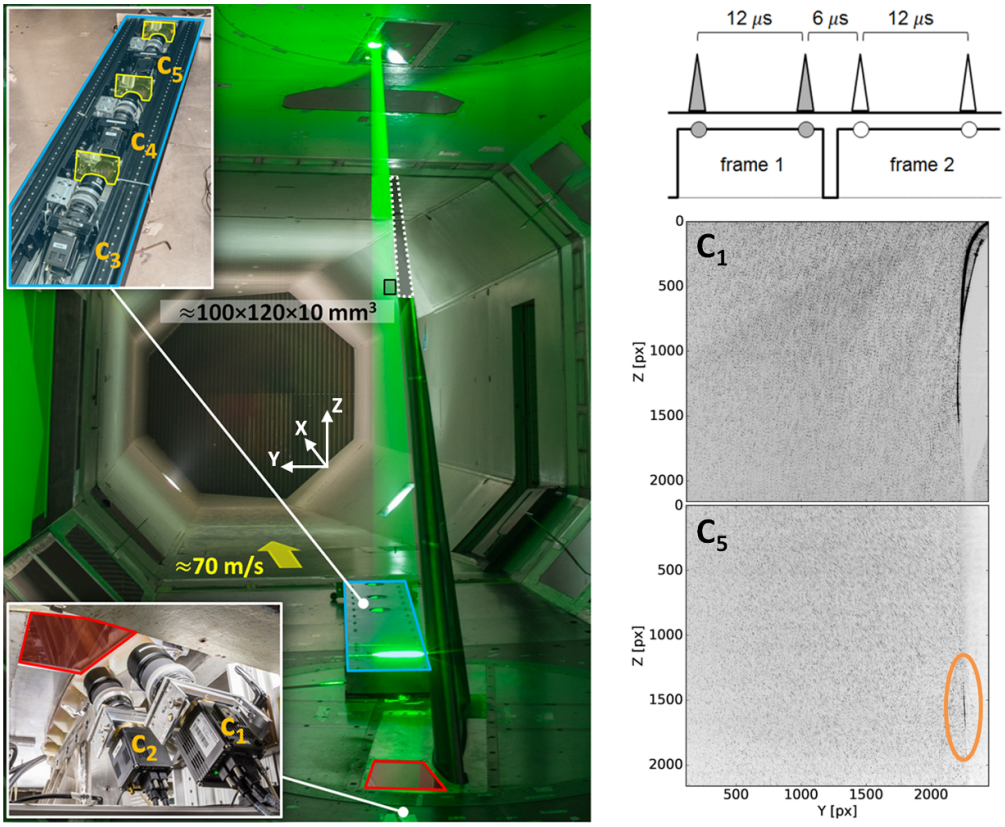

Figure 1: *Left*: experimental setup at the Airbus UK LSWT; winglet area blanked due to confidentiality (dashed white line). The yellow areas in the top-left image indicate mirrors placed in front of the downstream-pointing cameras (c_3, c_4, c_5) in order to obtain the desired field-of-view (black rectangle). *Right-top*: timing diagram for double-exposed multi-pulse recordings. *Right-bottom*: sample images from the most upstream (c_1) and the most downstream (c_5) cameras; the orange circle indicates the reflection of the model surface for c_5.

experimental data for validation of numerical methods. A half-wing model is installed in the test section of the closed loop facility; the model is approximately 2.6 m long in the span-wise direction (Z) and the airfoil cord is 1.1 m at the root. The model is installed onto a rotating plate that allows to change the angle of attack, figure 1-left. Several configurations in terms of angle of attack and wing tip geometry have been investigated; the details regarding the model geometry cannot be given here due to a confidentiality agreement. The origin of the coordinate system is located upstream of the model; the X axis is aligned with the incoming flow direction, the Y axis is normal to the airfoil chord at zero angle of attack and the Z axis is normal to the test section floor. The incoming flow velocity is approximately 70 m/s; the flow is seeded with DEHS droplets with a diameter of 1 μm.

Illumination is provided by two dual-cavity BigSky Evergreen 200 lasers installed on a rotating plate located above the roof of the test section. The rotation of this plate is synchronized with the rotation of the turntable where the model is installed; as a consequence, the relative position of the illuminated domain and the model does not change when varying the angle of attack. The laser sheet thickness is aligned with the flow direction (X axis) and it is set to 10 mm and 3 mm for the Multi-Pulse Shake-The-Box (MP-STB, Novara et al. (2016b)) and the stereo-PIV (Willert (1997)) measurements respectively.

For the MP-STB measurement, the emission of the two lasers is staggered to generate a sequence of four pulses over a time interval of 30 μs, figure 1-top-right. Following Novara et al. (2019), the pulses are unevenly distributed in order to increase the measurement dynamic range without compromising the accuracy of the particle tracking over the four-pulse sequence; a larger time interval is set between the first two and last two pulses ($\Delta t_{12} = \Delta t_{34} = 12\,\mu s$), while a smaller time interval is chosen between the second and third pulse ($\Delta t_{23} = 6\,\mu s$). On the other hand, for the stereo-PIV measurement, the laser system is configured to deliver two pulses separated by a time interval of 8 μs.

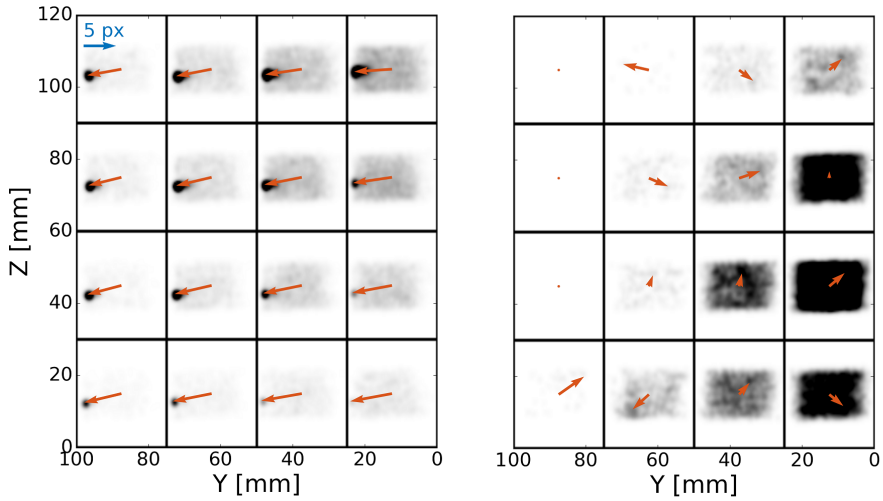

Figure 2: Disparity maps from VSC (first correction after target calibration) for camera c_2 relative to the central sub-volume along the depth direction. *Left*: results from ensemble VSC performed in wind-off condition. *Right*: unsuccessful single-image VSC for an instantaneous recording acquired during wind-tunnel operation.

The acquisition frequency for both the four-pulse and double-pulse recording sequences is $15\,Hz$; sequences of $100,000$ and $10,000$ recordings were acquired for the MP-STB and stereo-PIV measurements respectively.

The imaging system consists of five $5.5\,Mpx$ PCO.Edge sCMOS dual-frame cameras equipped with $180\,mm$ Zeiss lenses and $2x$ teleconverter resulting in $f = 360\,mm$ ($f_\# = 11$). The field-of-view (FOV) is shown in figure 1-left (black rectangle) and spans $100\,mm$ and $120\,mm$ in the surface-normal and the spanwise directions respectively; the digital resolution is $23\,px/mm$. The particle image density varies between $0.01\,ppp$ and $0.05\,ppp$. For the MP-STB measurement each frame is double-exposed in order to record the four laser pulses, figure 1-top-right. All cameras are installed on supports connected to the rotating plate carrying the model; as a consequence, the position of the FOV remains unchanged when varying the angle of attack.

The two cameras located upstream of the model (c_1, c_2) are installed on the turntable support below the test section; the optical access is granted by a glass-window installed on the wind-tunnel floor (in red in figure 1-left). In order to guarantee an optimal aperture angle of the imaging system, suitable for 3D particle triangulation and stereoscopic reconstruction, the remaining three cameras are installed downstream of the model. Nevertheless, due to the large sweep angle of the wing, the geometry of the room below the wind-tunnel floor and the lack of optical access, the cameras had to be installed inside the test section. In order to minimize obstruction, the cameras are mounted flat onto the floor, oriented towards the downstream direction and enclosed in a box (in blue in figure 1-left); a mirror (in yellow in figure 1-left) is positioned in front of each camera lens in order to obtain the same FOV of c_1 and c_2. At its upstream end the box is fixed to the rotating plate, while, at the downstream end, it is supported by a wheeled carriage allowing the cameras to rotate with the model.

The imaging system is calibrated making use of a 3D calibration target; since both the illumination and imaging systems follow the model rotation, a single target calibration can be used for all the investigated configurations. Volume self-calibration is performed making use of dedicated single-exposed particle images recorded in wind-off conditions before and after the actual measurements. Following the method proposed by Wieneke (2008), a successful VSC correction can be carried out for all dedicated VSC runs; the 3D domain is partitioned in $4 \times 4 \times 3$ sub-volumes in the Y, Z and X directions respectively, and an iterative ensemble averaging approach is followed to reduce the decalibration error from a few pixels ($\approx 5\,px$) down to less than $0.1\,px$. An example of the disparity maps obtained from the first VSC correction after target calibration is shown in figure 2-left for camera c_2 at the central sub-volume along the depth direction (X); the disparity maps, evaluated in the pixel space (i.e. image plane uv), are visualized at the location of the corresponding 3D sub-volume together with the disparity vector. A maximum allowed triangulation error of $6\,px$ was used and the disparity maps were summed over 20 instantaneous recordings; the particle disparities cluster in well-defined peaks and the disparity vectors indicate a consistent shift across the vol-

ume which is compatible with a drift of the camera system with respect to the target calibration. The optical transfer function (OTF, Schanz et al. (2012)) is also estimated during the volume self-calibration process.

The successful application of the VSC correction for the dedicated runs in wind-off conditions, before and after the actual measurement runs, indicates that the imaging system is relatively stable; after the wind-tunnel operation, all cameras, possibly undergoing unsteady displacements as a consequence of the aerodynamic loads (exerted on those placed in the test section), structural vibrations and the change of angle of attack, return to a position where a calibration error lower than $10\,px$ can be easily identified and corrected for by means of ensemble VSC.

On the other hand, when the VSC is performed using single instantaneous recordings acquired during wind-tunnel operation, figure 2-right, the disparity maps are dominated by noise and a clear peak cannot be identified. In order to account for relatively large camera shifts, the maximum allowed triangulation error was increased (up to $15-20\,px$, a further increase being practically unattainable due to the dramatic increase in the number of ghost particles) and only a relatively small percentage of the brightest 2D particle peaks ($\approx 10\%$) was selected for triangulation; nevertheless, a coherent disparity map could not be obtained for any of the analyzed instantaneous recording. Clearly, unlike for the wind-off case, the iterative application of the disparity maps shown in figure 2-right does not result in a progressive decrease of the residual disparity error, confirming the failure of the single-snapshot VSC approach. In these conditions, not only the analysis of the data by means of MP-STB or stereo-PIV cannot be carried out, but also the magnitude of the calibration error remains unknown.

An alternative tailored approach to detect and correct for large unsteady camera decalibration has been implemented and it is presented in the following section.

3 Instantaneous volume-self calibration approach

A novel approach is implemented in order to detect and compensate for the unsteady decalibration error for each snapshot in the recording sequence; the same strategy is adopted for both the four-pulse recordings used for 3D LPT with Multi-Pulse STB, and for the double-pulse recordings for stereo-PIV.

The proposed method is tailored to the particular arrangement of the imaging system described in section 2, where three of the five cameras are installed within the wind-tunnel test section. As a consequence of the aerodynamic loads exerting onto these cameras, and of the structural vibrations involving the complete imaging system, a strong unsteady decalibration is expected when the complete imaging system is considered. On the other hand, it can be assumed that significantly smaller relative shifts occur between the three downstream cameras (c_3, c_4, c_5), which are installed onto the same support enclosed in a relatively sturdy box, figure 1-left; the same assumption can be made regarding cameras c_1 and c_2.

This assumption can be verified for cameras c_3, c_4, c_5 as the three cameras can be considered as part of an individual 3D imaging sub-system that can be successfully calibrated by means of a single-image VSC approach similar to what proposed by Michaelis and Wolf (2011), (section 3.1).

Subsequently, the IPR technique is performed using the calibrated system c_3, c_4, c_5 to reconstruct the 3D particle locations, and the reconstructed particle peaks are back-projected onto the image planes of the two upstream cameras c_1, c_2. This step is performed making use of the mapping functions from target calibration; as a consequence, the shift between the back-projected peaks and the recorded particle images is representative of the calibration error between c_1, c_2 and the downstream camera system. This shift is detected by means of 2D cross-correlation performed with the Particle Space Correlation (PSC, Novara et al. (2016a)), and used to correct the mapping functions of cameras c_1, c_2 (section 3.2).

After this correction, the complete imaging system can be calibrated by means of single-image VSC adopting a relatively small maximum allowed triangulation error (section 3.3).

3.1 Single-image VSC of the downstream three-camera sub-system

For each individual snapshot in the recording sequence a single-image VSC is performed making use of the particle images from c_3, c_4, c_5; three VSC iterations are used, where the maximum allowed triangulation error is progressively reduced from $15\,px$ to $1\,px$. A single sub-volume is used along the depth direction while the number of sub-volumes along the Y and Z axis is increased from 2×2 to 4×4 after the first disparity correction. In order to reduce the effect of ghost particles, a decreasing intensity threshold for the identification of the 2D particle peaks is employed, which results in the detection of 10%, 30% and 60% of the total number of recorded peaks for the three VSC iterations respectively.

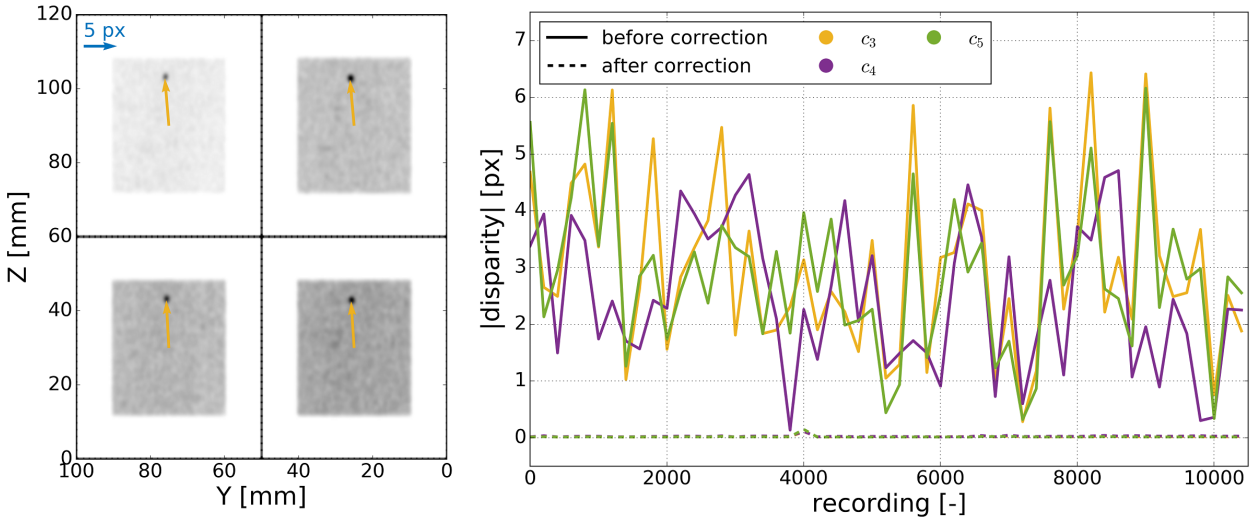

Figure 3: *Left*: instantaneous disparity map for camera c_3 (first VSC iteration) obtained from an actual recording during wind-tunnel operation. *Right*: time-history of the disparity before and after single-image VSC correction for the downstream camera system (c_3, c_4, c_5).

An example of instantaneous disparity map is shown in figure 3-left for camera c_3. As a consequence of the large triangulation radius the disparity maps exhibit a relatively high noise level; nevertheless, the clear disparity peak and the consistent direction of the disparity vector over the sub-volumes suggest a successful VSC analysis.

The time-history of the disparity magnitude over a sequence of $10,000$ recordings is shown in figure 3-right for the three cameras in the sub-system. An unsteady decalibration up to approximately 7 px can be observed (solid lines), while the accuracy of the VSC correction is confirmed by the low magnitude of the residual disparity (< 0.1 px) after the third VSC iteration is performed (dashed lines).

As a consequence, after application of single-image VSC for each realization in the recording sequence, the imaging sub-system formed by cameras c_3, c_4, c_5 can be considered as accurately calibrated.

3.2 Upstream cameras shift detection with Particle Space Correlation

The particle images from the calibrated downstream camera sub-system are used to reconstruct the 3D particle distribution with IPR (Wieneke (2013)). A triangulation error of 1 px and a relatively high intensity threshold for the 2D peaks are used in order to reduce the number of ghost particles; 20% of the brightest particle peaks are used for triangulation, resulting in approximately $15,000$ triangulated particles.

The 3D particle peak positions are then back-projected onto the image plane of cameras c_1 and c_2 making use of the mapping functions obtained from target calibration, and the shift between the back-projected locations and the recorded particle peaks is detected by means of Particle Space Correlation (PSC, Novara et al. (2016a)). The PSC operates similarly to the window deformation iterative cross-correlation approach proposed by Scarano and Riethmuller (2000), but, instead of making use of the image intensity discretized in pixels, employs only the particle peak locations and intensities. A portion of the image plane of approximately 1000×1000 px, located within the active part of the sensor, is divided into 400×400 px correlation windows with a 50% overlap factor; a large search radius of 200 px is set in order to detect the potential large decalibration shift between the upstream cameras and those placed within the test section.

An example of the disparity map obtained from PSC for an instantaneous recording is shown, for camera c_2, in figure 4-left (black vectors); the uniform direction of the disparity vectors over the 2D image plane is compatible with a large shift between the cameras located within the test-section and the ones positioned outside. For each disparity map (i.e. for each of the two upstream cameras and instantaneous recording) a single shift in the image plane uv is obtained as the average decalibration error (orange vector in figure 4-left) and used to shift the uv position of the origin of the camera reference system, previously obtained from target calibration.

The time-history of the decalibration shift magnitude is shown in figure 4-right for the two upstream cameras (solid lines); as expected, a large unsteady decalibration between the two sets of cameras is found

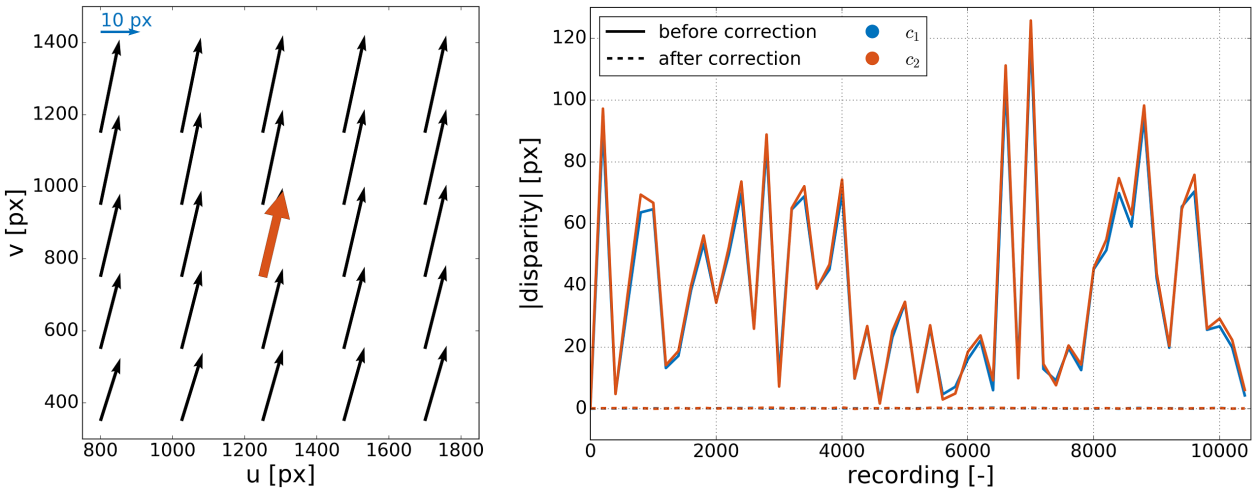

Figure 4: *Left*: instantaneous disparity between back-projected reconstructed particle locations (IPR with c_3, c_4, c_5) and recorded particle peaks for camera c_2. Disparity map detected by 2D-PSC in black; mean decalibration shift used to correct the camera position in orange. *Right*: time-history of the decalibration shift between cameras c_1, c_2 and the sub-system formed by c_3, c_4, c_5 before and after correction.

(up to $\approx 120\,px$), which could not be detected by the standard VSC approach adopted for the results shown in figure 2. The possibility of correcting for such a shift by means of the advanced VSC methods proposed by Wieneke (2018), reportedly proven effective up to and exceeding $\approx 30\,px$, is not investigated in the present study and could be the subject of a future work.

A similar decalibration magnitude is found for cameras c_1, c_2, which confirms the hypothesis that most of the decalibration error is due to the different location of the upstream and downstream cameras, respectively outside and inside the test section; conversely, the relative calibration error within the two sets of cameras is lower than $10\,px$.

A second iteration of IPR reconstruction, back-projection and shift detection with 2D-PSC shows that, after the correction of the camera position, the residual disparity shift magnitude is reduced to sub-pixel values (dashed lines in figure 4-right).

3.3 Instantaneous VSC of the complete imaging system

The final step of the instantaneous self-calibration scheme consists in the single-image VSC of the complete imaging system; this is needed in order to correct for the residual disparity that could not be compensated for by the single shift correction of the c_1, c_2 cameras position described in section 3.2.

For each individual snapshot the particle images from all five cameras are used to perform three VSC iterations; the maximum allowed triangulation error is set to $2\,px$ for the first two iterations and reduced to $1\,px$ for the last correction. The relatively low triangulation error allows for the adoption of a lower intensity threshold for the identification of the 2D particle peaks, resulting in approximately 90% of the recorded particle images being used during the 3D triangulation step of the VSC. For all three VSC iterations the volume is partitioned in $5 \times 5 \times 1$ sub-volumes along the Y, Z and X directions respectively.

An instantaneous disparity map for one of the cameras in the imaging system (c_2) is shown in figure 5-left; the disparity maps exhibit a relatively low noise level and the disparity peaks can be clearly identified. As indicated by the time-history of the disparity magnitude for all cameras along a sequence of $10,000$ recordings, the calibration error is well within the sub-pixel range ($< 0.6\,px$, solid lines in figure 5-right) and can be corrected down to less than $0.1\,px$ (dashed lines), a suitable value for both accurate 3D particle reconstruction with IPR within the MP-STB processing and for the evaluation of the out-of-plane velocity component in stereoscopic PIV.

It can be concluded that the present approach for instantaneous self-calibration (based on single-image VSC, 3D particle reconstruction and back-projection of the reconstructed peaks onto the image plane) allowed for the detection of unsteady decalibration errors up to and exceeding $100\,px$ ($\approx 4.5\,mm$) and for the correction of the detected disparity down to the sub-pixel range ($< 4\,\mu m$), as typically accepted for 3D investigations with multi-camera imaging systems.

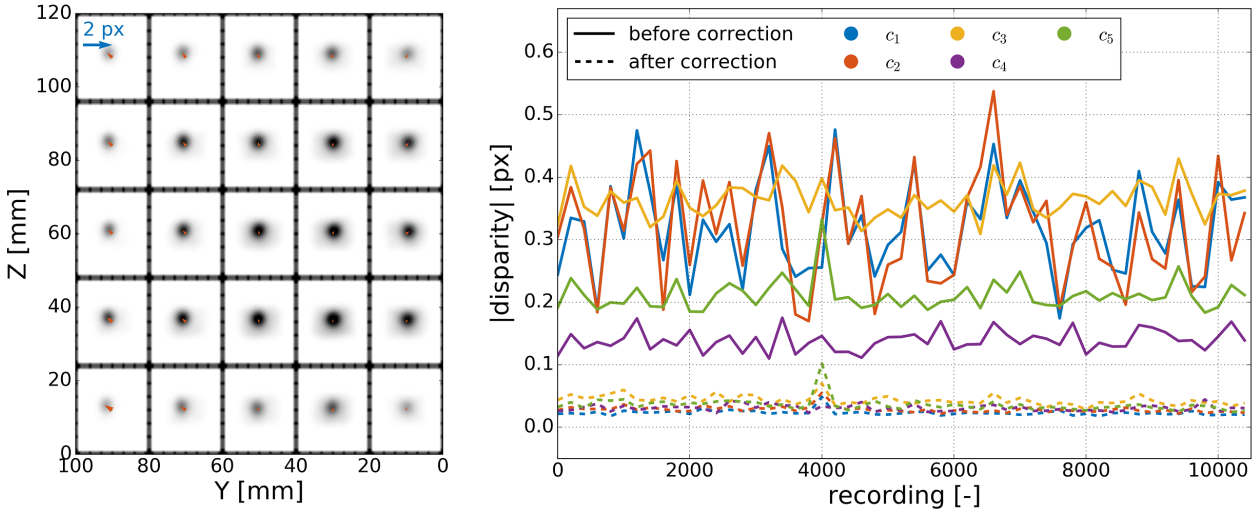

Figure 5: *Left*: result from the first iteration of single-image VSC for the complete five-cameras imaging system making use of an actual recording during wind-tunnel operation; disparity map for camera c_2. *Right*: time-history of the disparity before and after single-image VSC correction of the complete imaging system.

4 Multi-Pulse Shake-The-Box and stereo-PIV results

The Multi-Pulse Shake-The-Box technique proposed by Novara et al. (2019) is applied here for the analysis of the double-exposed multi-pulse recordings. For each instantaneous recording, the mapping functions of the five cameras in the imaging system are corrected following the approach presented in section 3. A single MP-STB iteration is performed; the IPR reconstruction of the two frames (namely IPR_{fr_1} and IPR_{fr_2}), containing pulses $1-2$ and $3-4$ respectively, is followed by an iterative particle tracking procedure.

Concerning the 3D particle reconstruction, a maximum allowed triangulation error of $0.9\,px$ is used; for the last two of the five IPR iterations, the triangulation is performed by successively excluding individual cameras to solve particle image overlap situations occurring for a single viewing direction.

The tracking scheme described by Novara et al. (2019) is adapted here to cope with the different distribution of the pulses along the sequence, figure 1-right-top. Two-pulse tracks are identified by means of a nearest neighbor approach; a search radius $\delta_{2p} = 20\,px$ is established around each particle in IPR_{fr_1} and possible matches are identified within IPR_{fr_2}. Since a maximum particle displacement of $\approx 15-17\,px$ is expected within $\Delta t_{23} = 6\,\mu s$, this step allows to identify two-pulse tracks between pulses $2-3$.

Subsequently, the two-pulse tracks are linearly extrapolated backward and forward (based on $\Delta t_{12} = \Delta t_{34} = 12\,\mu s$) in order to establish the center of search regions used to extend the tracks to pulses 1 and 4 respectively. A search radius $\delta_{4p} = 3\,px$ is chosen; when particles in IPR_{fr_1} and IPR_{fr_2} are found within these areas, two-pulse tracks are extended to form four-pulse track candidates.

Tracks are defined by filtering out spurious track candidates. A linear fit for the particle locations along the sequence is performed; a criterion based on the maximum residual from the fit is employed and, when multiple candidates share the same particle, the candidate exhibiting the minimum residual is chosen (Schanz et al. (2016), Novara et al. (2016b), Novara et al. (2019)). A second order polynomial is used to fit the individual particle tracks; position, velocity and acceleration are extracted at the center of the track, where the accuracy of the track fit is higher (Novara et al. (2019)).

The tracks identified in this first iteration are used as a predictor for two further iterations, where the search radius δ_{4p} is increased up to $12\,px$ in order to capture strong acceleration events; due to the availability of a predictor for the particle displacement, the two-pulse search radius δ_{2p} can be reduced to $6\,px$, lowering the chance of generating spurious tracks.

Due to the relatively thin volume ($10\,mm$), aligned with the stream-wise direction X, a significant number of tracks enters (or leaves) the illuminated domain within the $30\,\mu s$ span of the four-pulse sequence. As a consequence, after the definition of the four-pulse tracks, an additional tracking iteration is performed where three-pulse tracks are identified within pulses $1-2-3$ and $2-3-4$. Depending on the instantaneous particle image density, varying between approximately $0.01\,ppp$ and $0.03\,ppp$, a total number of $15,000$ to $40,000$ tracks are found, evenly shared between three- and four-pulse tracks.

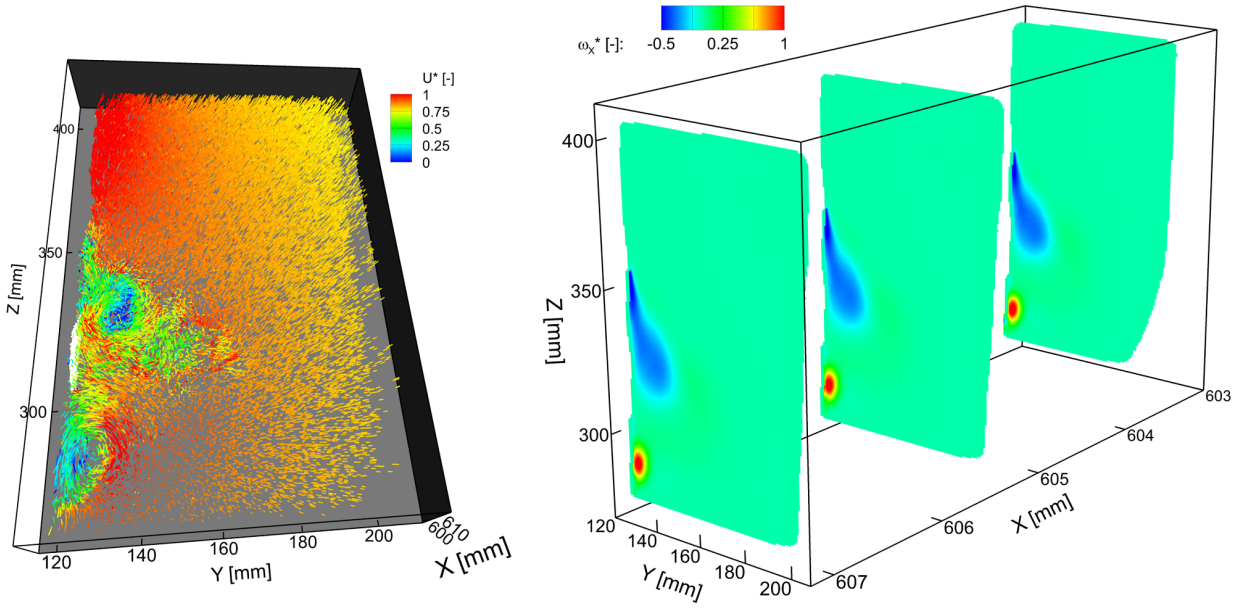

Figure 6: *Left*: instantaneous MP-STB result. Approximately 29,000 instantaneous tracks color-coded by normalized stream-wise velocity component; reconstruction of the model surface reflection in white. *Right*: average normalized stream-wise vorticity component obtained from ensemble averaging of the instantaneous MP-STB tracks over 100,000 statistically independent recordings.

For the stereo-PIV evaluation of the single-exposed dual-pulse recordings, cameras c_1 and c_5 are chosen due to the large aperture angle, suitable for the evaluation of the out-of-plane velocity component. An iterative multi-grid 2D cross-correlation approach with window deformation is carried out using PIV-view3.0 (Pivtec, http://www.pivtec.com); the correlation window size is progressively reduced from $128 \times 128\,px$ to $32 \times 32\,px$ (66% overlap). The 2D-2C velocity fields are then combined into 2D-3C fields (Willert (1997)) according to the instantaneous corrected calibration of the imaging system.

Due to a confidentiality agreement with Airbus, all quantities presented in this section are normalized.

An instantaneous result from MP-STB is presented in figure 6-left; approximately 29,000 tracks are shown, color-coded by the stream-wise velocity component. As shown in figure 1-right, significant reflections from the model surface are present on the camera images; these areas are masked before processing to avoid noise in the particle reconstruction. As the location of the reflections on the camera images is displaced due to the unsteady vibrations of both the cameras and the model, reflections are automatically detected and masked for each instantaneous recording.

On the other hand, the reflection regions are used as input for a further IPR reconstruction in order to provide an instantaneous reference for the location of the model surface. Since the surface of the model is curved, different reflections are seen from different viewing angles; as a consequence, only cameras c_3, c_4, c_5 (which share a similar viewing direction) are used for the reconstruction. The reconstruction of the reflection area indicated with an orange circle in figure 1-right is shown in white in figure 6-left.

Due to the magnitude of the instantaneous VSC correction, a significant unsteady shift of the origin of the coordinate system is introduced (Cornic et al. (2016)), resulting in an artificial displacement of the reconstructed fields along the recordings sequence. The reconstructed surface reflection is used as a reference position for the model, and the instantaneous MP-STB tracks (as well as the 2D-3C fields from stereo-PIV) are relocated within the 3D space in order to correct for the artificial coordinate shift. Furthermore, this correction allows to place the measurement fields at the same position with respect to the (vibrating) model surface. As a consequence, the flow statistics can be evaluated by averaging over the full recording sequences without introducing spurious fluctuations due to positional errors of the measurement volume.

An ensemble averaging approach is used for the MP-STB results. Instantaneous measurement points are extracted at the tracks mid-point and collected into $16 \times 16\,px$ bins ($0.7 \times 0.7\,mm^2$) in the YZ plane; along the X direction, the volume is partitioned in three 47 px bins ($2\,mm$) in order to capture the stream-wise evolution of the flow. On average, 20,000 samples per bin are available when considering the complete 100,000 recordings sequence.

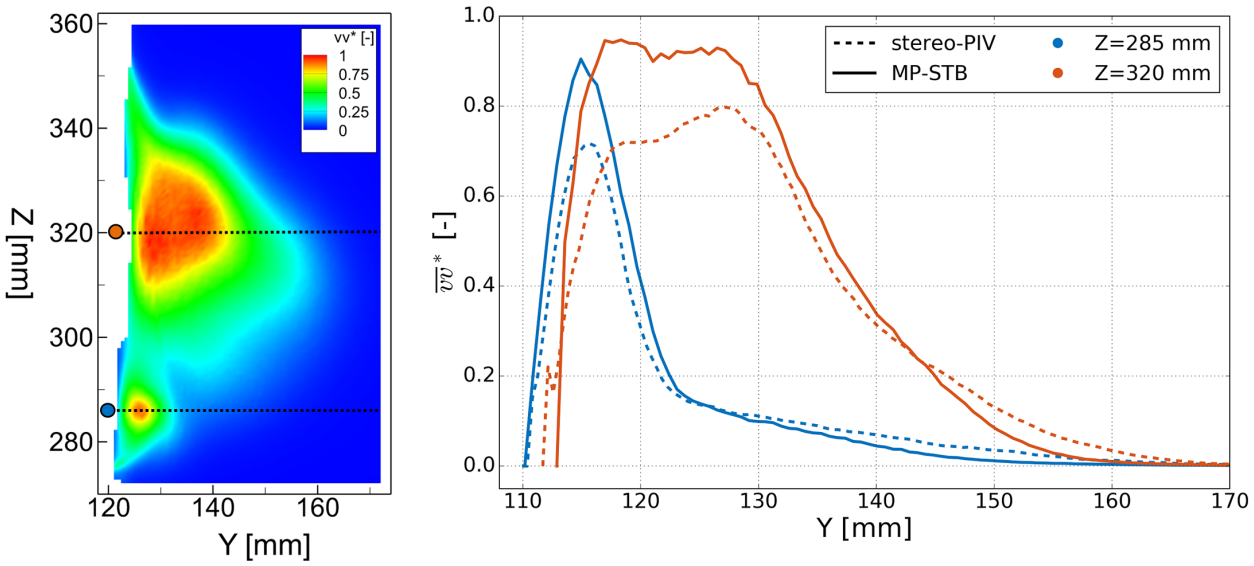

Figure 7: *Left*: wall-normal Reynolds stress component at $X = 605\,mm$ obtained from ensemble averaging of the MP-STB results; black lines indicate the location of the profiles shown on the right. *Right*: wall-normal component of the Reynolds stresses at two span-wise locations ($Z = 285/320\,mm$); comparison between MP-STB and stereo-PIV results.

The mean stream-wise vorticity component is presented in figure 6-right; this result confirms the presence of two counter-rotating vortical structures in the near wall region which can also be identified in the instantaneous track field. The wall-normal component of the Reynolds stresses is presented in figure 7-left for the bottom-left portion of the domain (central bin along the stream-wise direction). Two profiles along the wall-normal direction are extracted at $Z = 285\,mm$ and $Z = 320\,mm$ (solid lines in figure 7-right) and the results are compared to those obtained with stereo-PIV at the same locations (dashed lines).

Both measurement techniques capture the main features of the flow, but the modulation effect introduced by the $32 \times 32\,px$ cross-correlation windows employed by the stereo-PIV is indicated by lower fluctuation values within the two main regions of turbulent activity ($Y \approx 115\,mm$ and $Y \approx 125\,mm$ for the $Z = 285\,mm$ and $Z = 320\,mm$ profiles respectively). On the other hand, lower $\overline{vv}^*$ values are found for the MP-STB results in the region away from the model surface ($Y > 150\,mm$), suggesting a lower noise level for the 3D Lagrangian particle tracking results.

5 Conclusions

A novel approach for the correction of unsteady calibration errors of a multi-camera 3D imaging system has been presented. The method is tailored to the arrangement of a five-cameras setup employed for the investigation of the flow on the suction side of a half wing model in a large industrial facility (LSWT at Airbus UK). Structural vibrations and aerodynamic loads exerted onto the imaging system (partially located within the wind-tunnel test-section) resulted in large calibration errors (up to $120\,px \approx 5\,mm$) which could not be corrected by means of standard volume self-calibration (VSC, Wieneke (2008)). The proposed approach (based on the application of single-image VSC, Michaelis and Wolf (2011), 3D Iterative Particle Reconstruction, IPR, Wieneke (2013), and 2D cross-correlation between back-projected and recorded particle peaks) allowed for the correction of the unsteady decalibration down to sub-pixels values ($< 0.1\,px \approx 4\,\mu m$). The calibrated imaging system has been employed for the investigation of the flow by means of 3D Lagrangian particle tracking with Multi-Pulse Shake-The-Box and stereoscopic PIV. Results are presented in terms of both instantaneous and average flow fields; the comparison of the MP-STB and stereo-PIV results confirms the suitability of Lagrangian particle tracking approaches for the investigation of near-wall flows exhibiting strong spatial gradients (Kähler et al. (2012)). The application of advanced VSC approaches (Wieneke (2018)), proven effective for calibration errors up to and exceeding $30\,px$, remains to be investigated and could be the subject of a future study.

6 Acknowledgements

The authors would like to thank the people from the Airbus LSWT facility in Filton (UK) and Airbus Operations GmbH for providing support during the experiments, and acknowledge Airbus for allowing the publication of the present data.

References

Cornic P, Illoul C, Cheminet A, Le Besnerais G, Champagnat F, Le Sant Y, and Leclaire B (2016) Another look at volume self-calibration: calibration and self-calibration within a pinhole model of scheimpflug cameras. *Measurement Science and Technology* 27:094004

Earl T, Cochard S, Thomas L, Tremblais B, and David L (2014) Implementation of vibration correction schemes to the evaluation of a turbulent flow in an open channel by tomographic particle image velocimetry. *Measurement Science and Technology* 26:015303

Elsinga G, Westerweel J, Scarano F, and Novara M (2011) On the velocity of ghost particles and the bias errors in tomographic-piv. *Experiments in fluids* 50:825–838

Elsinga GE, Scarano F, Wieneke B, and van Oudheusden BW (2006) Tomographic particle image velocimetry. *Experiments in fluids* 41:933–947

Kähler CJ, Scharnowski S, and Cierpka C (2012) On the uncertainty of digital piv and ptv near walls. *Experiments in fluids* 52:1641–1656

Michaelis D and Wolf C (2011) Vibration compensation for tomographic piv using single image volume self calibration. in *Proceeding of the 9th International Symposium on Particle Image Velocimetry, Kobe, Japan*. pages 21–23

Novara M, Schanz D, Geisler R, Gesemann S, Voss C, and Schröder A (2019) Multi-exposed recordings for 3d lagrangian particle tracking with multi-pulse shake-the-box. *Experiments in Fluids* 60:44

Novara M, Schanz D, Gesemann S, Lynch K, and Schröder A (2016a) Lagrangian 3d particle tracking for multi-pulse systems: performance assessment and application of shake-the-box. in *18th International Symposium on Applications of Laser Techniques to Fluid Mechanics*. pages 4–7

Novara M, Schanz D, Reuther N, Kähler CJ, and Schröder A (2016b) Lagrangian 3d particle tracking in high-speed flows: Shake-the-box for multi-pulse systems. *Experiments in Fluids* 57:128

Scarano F and Riethmuller ML (2000) Advances in iterative multigrid piv image processing. *Experiments in Fluids* 29:S051–S060

Schanz D, Gesemann S, and Schröder A (2016) Shake-the-box: Lagrangian particle tracking at high particle image densities. *Experiments in fluids* 57:70

Schanz D, Gesemann S, Schröder A, Wieneke B, and Novara M (2012) Non-uniform optical transfer functions in particle imaging: calibration and application to tomographic reconstruction. *Measurement Science and Technology* 24:024009

Wieneke B (2005) Stereo-piv using self-calibration on particle images. *Experiments in fluids* 39:267–280

Wieneke B (2008) Volume self-calibration for 3d particle image velocimetry. *Experiments in fluids* 45:549–556

Wieneke B (2013) Iterative reconstruction of volumetric particle distribution. *Measurement Science and Technology* 24:024008

Wieneke B (2018) Improvements for volume self-calibration. *Measurement Science and Technology*

Willert C (1997) Stereoscopic digital particle image velocimetry for application in wind tunnel flows. *Measurement science and technology* 8:1465